2026 IEEE International Conference on Robotics and Automation (ICRA 2026)
June 1-5, 2026. Vienna, Austria

A Hybrid Magnetic Actuation System for Hybrid Microrobotic Targeted Delivery

Yuanbiao Ma[1,2],Shengming Luo[1,2], Bin Wang[1,2], Haoyu Zhang[1,2], Ji Lang[1,2], Zhiqiang Tang[1,2], Li Zhang[3,4,5,6], *Fellow, IEEE* and Qianqian Wang[1,2], *Senior Member, IEEE*

***Abstract*— Magnetic microrobots hold great promise for biomedical applications. However, achieving flexible magnetic field adjustment with a magnetic actuation system (MAS) to actuate diverse microrobots remains a significant challenge. In this work, we propose an Electromagnetic–Permanent Magnet Actuation (EPMA) system that generates controllable magnetic field variations to enable microrobot actuation for diverse tasks, including microrobotic actuation, microswarm pattern transformation and targeted delivery. Automatic ellipsoid calibration of the Hall sensors enables real-time magnetic field orientation measurement with an error under 3°. Experimental results demonstrate the microrobot's actuation performance in four distinct scenarios, with a rotation frequency of 0.5 Hz. Furthermore, by adjusting the dynamic magnetic field, we achieve microswarm pattern reconfiguration under static conditions as well as targeted delivery in fluidic environments at a flow speed of 52 mm/s and a rotation frequency of 4 Hz. This study presents a hybrid MAS for the microrobotic actuation in diverse environments by controllable dynamic magnetic fields.**

I. Introduction

Magnetic microrobots and microswarms are promising tools in biomedicine. They offer unique advantages in minimally invasive procedures and precise control at the microscale. These systems can navigate through confined and complex environments [1]–[4]. This capability makes them suitable for applications such as targeted drug delivery, thrombus removal, vascular embolization, and microsurgery [5]–[10]. However, the complex and heterogeneous nature of biological tissues makes direct delivery to the targeted site difficult. Magnetically actuated capsules or catheters can transport microrobots to the vicinity of the target site, where smaller magnetic microrobots or microswarms are released for precise localized delivery. Each stage requires distinct magnetic field configurations for effective actuation. The design of magnetic actuation systems (MASs) capable of generating multiple magnetic field modes for these stages has not been fully investigated. Precise spatial magnetic field control is also essential for improving delivery efficiency and accuracy. Advances in MAS can enhance the dynamic control of microrobots. They can also improve delivery performance and increase the potential for clinical applications [11]–[13].

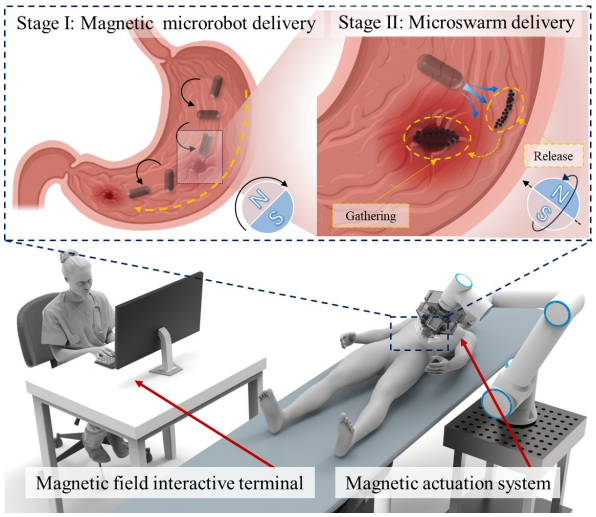

Fig. 1. Overview of the proposed EPMA system. The system is mounted on a 6-DOF collaborative robot, generating a dynamic magnetic field to actuate different stages of the magnetic microrobot's delivery. In Stage I, the microrobot is mainly actuated by magnetic torque, allowing it to navigate obstacles and uneven surfaces. In Stage II, the microswarm is released and guided to the target using both magnetic torque and gradient force, with the magnetic field and collaborative robot movement tuned via an interactive terminal.

The magnetic field strength and dynamic performance are critical for remote actuation of microrobots. Existing MASs are mainly categorized into electromagnetic actuation systems (EMASs) and permanent magnet actuation systems [14]–[19]. These MASs are essential for enabling microrobots to achieve diverse motion modes, allowing them to traverse complex terrains and accomplish targeted delivery tasks. Moreover, by adjusting the magnetic field, MASs can also realize pattern transformation and controllable navigation of microswarms. The OctoMag system is an EMAS designed for five-degree-of-freedom (5-DOF) wireless micromanipulation. It is capable of controlling the 3-DOF position and 2-DOF pointing orientation of a fully untethered microrobot [20]. The Advanced Robotics for Magnetic Manipulation (ARMM) system integrates a mobile electromag-

The work is supported by the National Natural Science Foundation under project no. 52575652. (*Yuanbiao Ma and Shengming Luo contributed equally to this work.*) (Corresponding author: Qianqian Wang and Li Zhang, Email: qqwang@seu.edu.cn, lizhang@mae.cuhk.edu.hk)

[1]Jiangsu Key Laboratory for Design and Manufacturing of Precision Medicine Equipment, School of Mechanical Engineering, Southeast University, Nanjing 211189, China.

[2]Department of Robotics, School of Mechanical Engineering, Southeast University, Nanjing, China.

[3]Department of Mechanical and Automation Engineering, The Chinese University of Hong Kong, Hong Kong, China.

[4] CUHK T Stone Robotics Institute, The Chinese University of Hong Kong, Hong Kong, China

[5] Chow Yuk Ho Technology Centre for Innovative Medicine, The Chinese University of Hong Kong, Hong Kong, China

[6] Multi-Scale Medical Robotics Center, Hong Kong Science Park, Hong Kong, China.

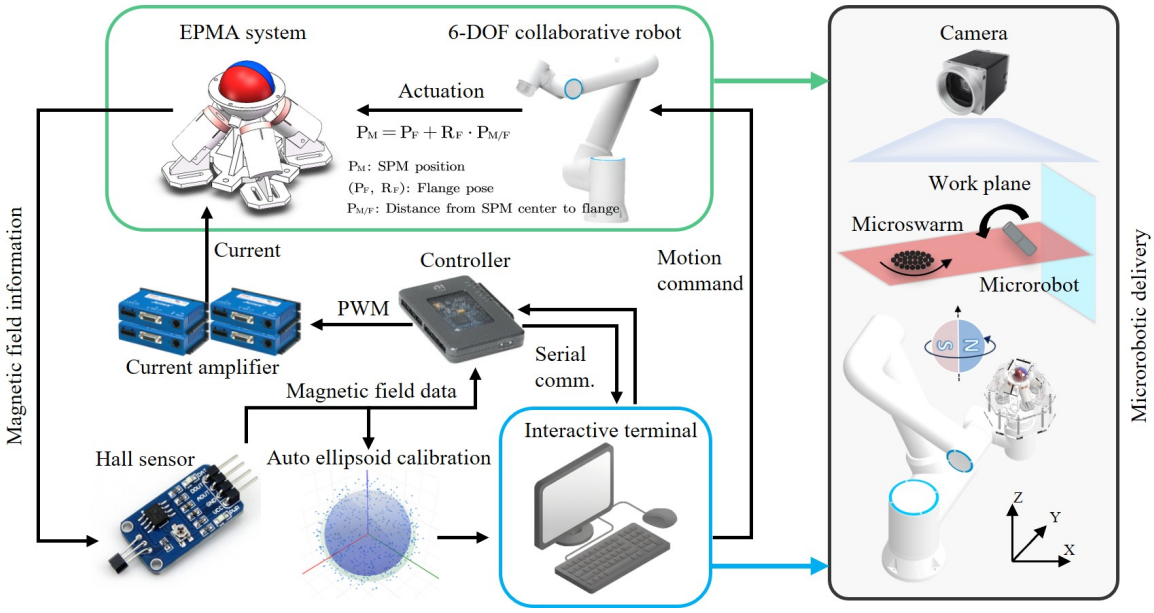

Fig. 2. Control framework of the microrobotic delivery system. High-level motion commands (interactive terminal) are processed by a central controller. The collaborative robot positions the EPMA system to generate precise magnetic fields for microrobot actuation. A Hall sensor array with ellipsoid calibration provides magnetic feedback for closed-loop control.

netic coil (EC) with a 6-DOF robotic arm, enabling large-workspace actuation of a magnetic endovascular catheter [21]. Using a rotating magnetic field generated by Helmholtz coils, the formation, pattern control, and navigation of microswarms can be achieved [22]. By employing different coil configurations, EMASs are capable of generating more flexible actuating magnetic fields. Permanent magnets are also widely used as magnetic resources in MASs. The Spherical-Actuator-Magnet Manipulator (SAMM) system overcomes magnetic manipulation limitations by decoupling the magnet's orientation from the robot's kinematics, achieving singularity-free actuation of microrobots [23]. A MAS with a rotating permanent magnet array has been developed, it can generate controllable three dimensional magnetic fields and gradients to achieve 5-DOF actuation of microrobot [24]. To address workspace limitations and restricted controllable DOFs, another MAS employing two permanent magnets collaboratively manipulated by robotic arms has been proposed, achieving independent 8-DOF actuation over two magnetic objects [25]. In addition, A hybrid MAS that integrates with ECs and a permanent magnet has been proposed, enabling scale reconfiguration and actuation of ferrofluidic microrobots [26]. However, the scenarios of these MASs remain limited, as they are typically designed for single-state actuation of a specific type of microrobot. There is still a lack of investigation on MASs for the actuation of microrobotic delivery across different stages and in different forms.

In this work, we propose an Electromagnetic–Permanent Magnet Actuation (EPMA) system (Fig.1), designed for microrobotic delivery in different stages. The purpose is to achieve both actuation and targeted aggregation of microrobots. The actuating magnetic field is generated by a spherical permanent magnet (SPM) with a diameter of ϕ 50 mm, which provides a stable and strong actuating magnetic field for actuation of microrobots. The rotation frequency and orientation of the SPM are precisely controlled by four ECs arranged symmetrically around it. This configuration enables the EPMA system to utilize a weak, controllable magnetic field to modulate and direct the strong magnetic field of the SPM, thereby achieving efficient and precise microrobot actuation.

II. Experimental System and Method

A. Electromagnetic and permanent magnet actuation model

The model objective is to manipulate the orientation of the SPM by generating a controllable magnetic field $\mathbf{B}$ using four ECs as shown in Fig.2. Since the working distance from the ECs to SPM surface is smaller than radius, the system operates in the near-field regime. During orientation control, the dominant effect is the pure magnetic torque applied to the SPM. Assuming the SPM has a uniform magnetization distribution and its magnetic moment is $\mathbf{m}$, the magnetic torque $\boldsymbol{\tau}$ can be approximated by the interaction between the magnetic moment and the controllable magnetic field $\mathbf{B}$ [27]

$$\boldsymbol{\tau} = \mathbf{m} \times \mathbf{B} \tag{1}$$

where $\mathbf{B}$ has a constant magnitude A and a direction represented by the unit vector $\hat{\mathbf{v}}$

$$\mathbf{B} = A\hat{\mathbf{v}} = A \begin{bmatrix} \sin p \cos d \\ \sin p \sin d \\ \cos p \end{bmatrix} \tag{2}$$

where p is the pitch angle and d is the direction angle.

The controllable magnetic field $\mathbf{B}$ is generated by the currents in the four ECs $\mathbf{I} = [I_1, I_2, I_3, I_4]^\top$. And the

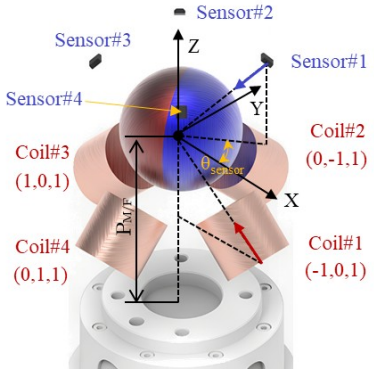

Fig. 3. The EPMA system. The setup includes a central SPM, four ECs (Coils#1–4) for actuation, and four Hall sensors (Sensors#1–4) for orientation sensing. The coordinate origin is at the center of SPM.

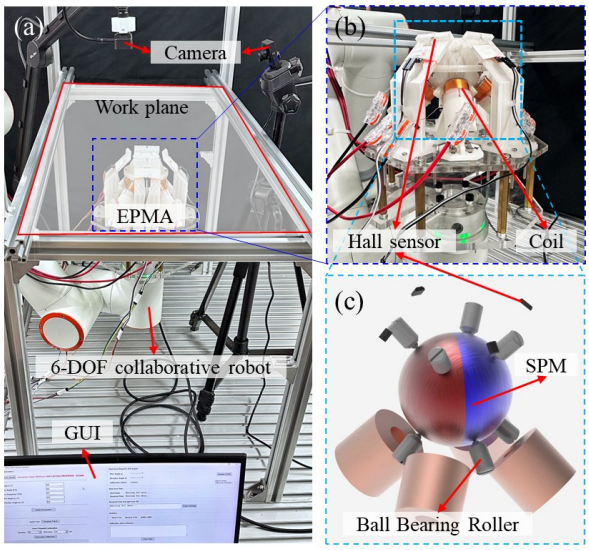

Fig. 4. Experimental setup. (a) The EPMA system is mounted on a 6-DOF collaborative robot beneath the work plane, with two cameras providing top and side views. Magnetic field parameters are monitored and adjusted through GUI. (b) The EPMA system prototype with four 1-DOF linear Hall sensors for real-time magnetic field monitoring. (c) Schematic of the SPM, electromagnetic coils, and Hall sensors. The SPM is housed in a spherical container with ball-bearing rollers to constrain its 3 translational DOFs.

direction of coil is mapped by a matrix $\mathbf{C} \in \mathbb{R}^{3\times4}$ shown in Fig.3

$$\mathbf{C} = \frac{1}{\sqrt{2}}\begin{bmatrix} -1 & 0 & 1 & 0 \\ 0 & -1 & 0 & 1 \\ 1 & 1 & 1 & 1 \end{bmatrix} \tag{3}$$

In this work, all four coils have identical physical parameters, the resulting magnetic field is proportional to the current. Since C has full column rank, the minimum norm current solution $(\min\|\mathbf{I}\|_2)$ to produce a desired magnetic field direction $\hat{\mathbf{v}}$ is given by the Moore-Penrose pseudoinverse

$$\mathbf{I}^* = \mathbf{C}^+\hat{\mathbf{v}} = \mathbf{C}^\top(\mathbf{C}\mathbf{C}^\top)^{-1}\hat{\mathbf{v}} \tag{4}$$

To account for the maximum current limits $\mathbf{I}_{\max}$ of the drivers and to avoid hardware overheating, the computed current $\mathbf{I}^*$ is scaled by

$$\mathbf{I} = \alpha \cdot \mathbf{I}^*, \quad \alpha = \frac{\max\left(|\mathbf{I}_i^*|\right)}{\mathbf{I}_{\max}} \tag{5}$$

To achieve controlled rotation, let the magnetic field vector $\mathbf{B}(t)$ generated by the ECs at time t rotate with angular frequency ω about a unit axis $\mathbf{u}$. According to the Rodrigues' rotation formula

$$\begin{aligned}\mathbf{B}(t) = A\big[&\hat{\mathbf{v}}\cos(\omega t) + (\mathbf{u}\times\hat{\mathbf{v}})\sin(\omega t) \\ &+ \mathbf{u}(\mathbf{u}\cdot\hat{\mathbf{v}})\big(1-\cos(\omega t)\big)\big]\end{aligned} \tag{6}$$

is satisfied

$$\mathbf{u} = \begin{bmatrix} \sin p_r \cos d_r \\ \sin p_r \sin d_r \\ \cos p_r \end{bmatrix} \tag{7}$$

B. Sensor ellipsoid calibration

The system uses four 1-DOF Hall sensors to estimate the orientation of the SPM as shown in Fig.2. For a uniformly SPM, the magnetic field $\mathbf{B}(\mathbf{r})$ at a position $\mathbf{r}$

$$\mathbf{B}_p(\mathbf{r}) = \frac{\mu_0}{4\pi}\left[\frac{3\mathbf{r}(\mathbf{m}\cdot\mathbf{r})}{r^5} - \frac{\mathbf{m}}{r^3}\right] \tag{8}$$

The four sensors are installed at an identical distance r from the SPM in Fig.3. The unit radial vectors $\hat{\mathbf{r}}$ of their respective positions are given by the matrix $\mathbf{R} \in \mathbb{R}^{4\times3}$

$$\mathbf{R} = \begin{bmatrix} \hat{\mathbf{r}}_1^\top \\ \hat{\mathbf{r}}_2^\top \\ \hat{\mathbf{r}}_3^\top \\ \hat{\mathbf{r}}_4^\top \end{bmatrix} = \frac{1}{\sqrt{2}}\begin{bmatrix} -1 & 0 & -1 \\ 0 & -1 & -1 \\ 1 & 0 & -1 \\ 0 & 1 & -1 \end{bmatrix} \tag{9}$$

Considering that the sensors are far from the ECs and the field of SPM is significantly stronger, the radial magnetic field component B_{p_i} at the i-th sensor position can be approximated as

$$B_{p_i} = \frac{\mu_0}{4\pi r^3}[3(\mathbf{m}\cdot\hat{\mathbf{r}}_i) - (\mathbf{m}\cdot\hat{\mathbf{r}}_i)] = \frac{2\mu_0}{4\pi r^3}(\mathbf{m}\cdot\hat{\mathbf{r}}_i) \tag{10}$$

Let $\mathbf{m} = M\cdot\hat{\mathbf{m}}$, where $\hat{\mathbf{m}} = [m_x, m_y, m_z]^\top$ is unit orientation vector. The vector of ideal sensor $\mathbf{B}_{\text{ideal}}$

$$\mathbf{B}_{\text{ideal}} = \begin{bmatrix} B_{p_1} \\ B_{p_2} \\ B_{p_3} \\ B_{p_4} \end{bmatrix} = \frac{2\mu_0}{4\pi r^3}\mathbf{R}\mathbf{m} = f(r)\begin{bmatrix} -m_x - m_z \\ -m_y - m_z \\ m_x - m_z \\ m_y - m_z \end{bmatrix} \tag{11}$$

where $f(r) = \frac{\sqrt{2}M\mu_0}{4\pi r^3}$ is a scalar constant. A linear transformation matrix $\mathbf{T} \in \mathbb{R}^{3\times4}$ is defined to reconstruct a vector $\mathbf{x}$ that is directly proportional to the orientation vector $\hat{\mathbf{m}}$ from the ideal sensor readings

$$\mathbf{x}_B = \mathbf{T}\mathbf{B}_{\text{ideal}} = f(r)\hat{\mathbf{m}} \propto \hat{\mathbf{m}} \tag{12}$$

is satisfied

$$\mathbf{T} = -\frac{1}{2}\begin{bmatrix} 1 & 0 & -1 & 0 \\ 0 & 1 & 0 & -1 \\ 1/2 & 1/2 & 1/2 & 1/2 \end{bmatrix} \tag{13}$$

Ideally, the locus of all possible $\mathbf{x}_B$ vectors would form a perfect sphere. In practice, sensor outputs are voltages

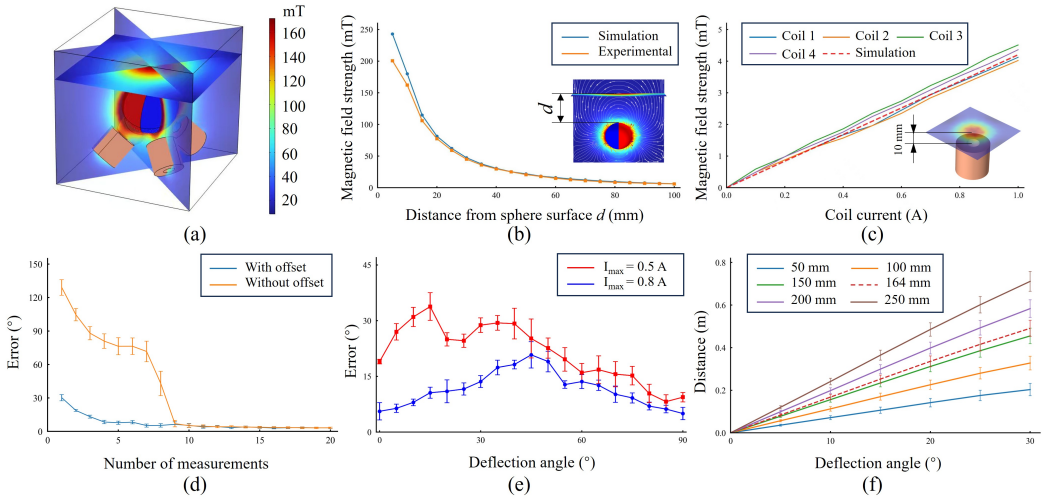

Fig. 5. (a) Simulation results of the magnetic field distribution of the EPMA system. (b) Magnetic field strength along the centerline of the SPM at distances d range from 5 to 100 mm. (c) Magnetic field strength at a distance of 10 mm from the electromagnetic coil with current varing from 0 to 1.0 A. (d) Orientation error versus number of measurement samples, with and without initial sensor offsets, under ellipsoid calibration. (e) the orientation error of the SPM at different deflection angles. (f) The sweep distance of the collaborative robot to achieve the desired deflection angles at various heights from the flange frame origin to the SPM. Error bars in (d–f) represent the standard error, calculated from 20, 6, and 6 trials, respectively.

TABLE I. Coil Parameter

Metric	Parameter
Inductance	6.0 mH
Resistance	7.0 Ω
Q factor	5.5
Wire diameter	0.4 mm
Number of turns	750
Inner dimension	10 mm
Outer dimension	25.8 mm
Height	25.5 mm

$\mathbf{V}$ and are affected by various error sources, including: (1) different gains and offsets for each sensor; (2) mechanical misalignments; and (3) non-uniform magnetization. The relationship between the actual sensor output voltages $\mathbf{V}$ and the ideal magnetic field readings $\mathbf{B}_{\text{ideal}}$ is modeled as an affine transformation

$$\mathbf{V} = \mathbf{G}\mathbf{B}_{\text{ideal}} + \mathbf{o} \tag{14}$$

where $\mathbf{G} = \text{diag}(g_1, g_2, g_3, g_4)$ is diagonal gain matrix and $\mathbf{o} = [o_1, o_2, o_3, o_4]^\top$ the offset voltage vector. Applying the transformation $\mathbf{T}$ to the measured voltages $\mathbf{V}$ gives the distorted reconstructed vector $\mathbf{x}_V$

$$\mathbf{x}_V = \mathbf{T}(\mathbf{G}\mathbf{B}_{\text{ideal}} + \mathbf{o}) = \underbrace{f(r)\mathbf{T}\mathbf{G}\hat{\mathbf{m}}}_{\mathbf{P}} + \underbrace{\mathbf{To}}_{\mathbf{b}} = \mathbf{P}\hat{\mathbf{m}} + \mathbf{b} \tag{15}$$

where $\mathbf{P} \in \mathbb{R}^{3\times3}$ is a distortion matrix and $\mathbf{b} \in \mathbb{R}^3$ is a offset vector.The gain g_i of each sensor is positive, and the sensors are placed in a non-coplanar, symmetric configuration, hence, $\mathbf{P}$ is invertible. Since $\hat{\mathbf{m}}$ is a unit vector, and $\hat{\mathbf{m}} = \mathbf{P}^{-1}(\mathbf{x} - \mathbf{b})$, we can get

$$(\mathbf{x} - \mathbf{b})^\top (\mathbf{P}^{-1})^\top \mathbf{P}^{-1}(\mathbf{x} - \mathbf{b}) = 1 \tag{16}$$

Define the ellipsoid matrix $\mathbf{W} \triangleq (\mathbf{P}^{-1})^\top \mathbf{P}^{-1}$. The equation becomes

$$(\mathbf{x} - \mathbf{b})^\top \mathbf{W}(\mathbf{x} - \mathbf{b}) = 1 \tag{17}$$

This defines an ellipsoid. The expanded quadratic form results in a general quadric [28] linearly parameterized by a parameter vector $\boldsymbol{\theta}$ and a regressor vector $\boldsymbol{\Phi}(\mathbf{x})$

$$\boldsymbol{\Phi}(\mathbf{x})^\top \boldsymbol{\theta} = 0 \tag{18}$$

where $\boldsymbol{\Phi}(\mathbf{x})$ and $\boldsymbol{\theta}$ contains the coefficients.

Given N calibration data points $\{\mathbf{x}_i\}_{i=1}^N$, the data matrix $\mathbf{D}$ is constructed with rows $\boldsymbol{\Phi}(\mathbf{x}_i)^\top$. The parameters are found by solving the constrained least-squares problem

$$\min_{\boldsymbol{\theta}} \|\mathbf{D}\boldsymbol{\theta}\|^2 \quad \text{subject to} \quad \mathbf{c}^\top \boldsymbol{\theta} = 1 \tag{19}$$

where $\mathbf{c} = [1, 1, 1, 0, 0, 0, 0, 0, 0, 0]^\top$ enforces a normalization on the quadratic terms. Finally, apply a rotation matrix to $\mathbf{P}$ for alignment with the Fig.3 reference frame.

III. Experimental Setup and Calibration

A. Experimental setup

Fig.4(a) provides an overview of the proposed EPMA system, which is deployed beneath the work plane for microrobotic actuation. The experimental setup includes two cameras that provide top and side views during experiments. The work plane serves as the base for placing the experimental platform. Mounted on the end of a 6-DOF collaborative robot, the EPMA gains an additional six degrees of freedom for generating the actuating magnetic field. A control program runs on a computer, enabling the operator to monitor the magnetic field and to send control commands through the GUI.

Fig.4(b)-(c) illustrate the EPMA system prototype and its internal configuration. The system employs a Grade-N35 NdFeB SPM with a diameter of ϕ50 mm, enclosed in a

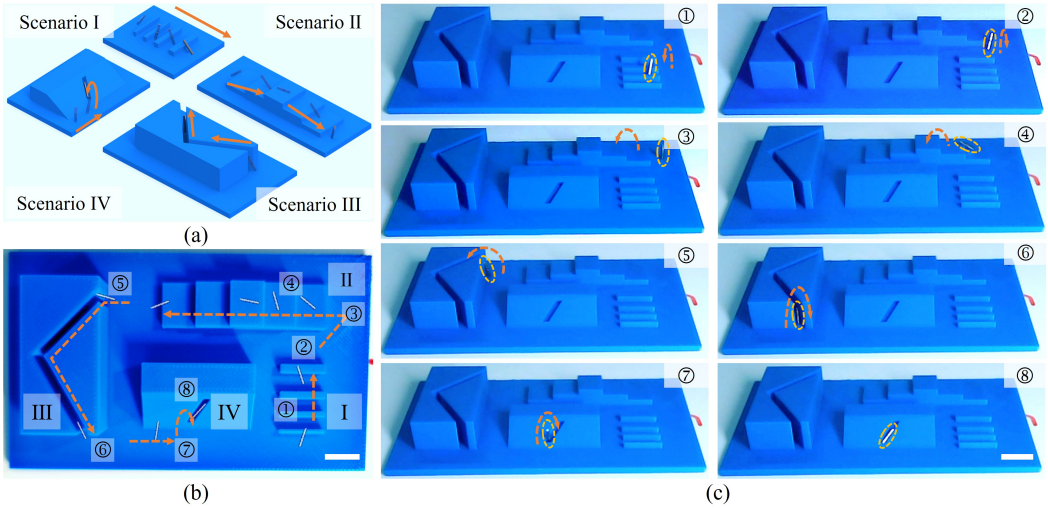

Fig. 6. Results of microrobot actuation on a rectangular platform with four different terrain environments. (a) Schematic of the four terrain environments, with the actuation process divided into four scenarios. Scenario I: Obstacle Overcoming, Scenario II: Stair Climbing, Scenario III: Narrow Path Crossing, Scenario IV: Gap Insertion. (b) Top view of the experimental platform and the motion path during microrobot actuation. Scenarios I-IV are denoted by I-IV, respectively. (c) Side view snapshots of the microrobot actuation. Orange arrow lines indicate the motion direction of the microrobot, curved arrow lines represent the roll direction, and dotted circles highlight the positions of the microrobot in different scenarios. The scale bars are 10 mm.

spherical container composed of two hemispherical shells. The translational 3-DOF of the SPM is constrained by eight ball-bearing rollers mounted inside the container. Four ECs (Table I) are evenly arranged beneath the SPM to generate a weak dynamic magnetic field for adjusting the SPM. Above the SPM, four 1-DOF linear Hall sensors are symmetrically arranged to measure its orientation.

B. Magnetic field characterization

The magnetic field distribution of the EPMA system is analyzed using finite element simulations in COMSOL Multiphysics. Fig 5(a) shows the simulated magnetic flux density generated by the EPFM system. The field strength is evaluated on planes located at distances d = 5-100 mm from the SPM surface. Corresponding experimental measurements are performed using a three-axis Hall sensor, and the results are presented in Fig.5(b) for comparison with the simulations. Furthermore, the magnetic field generated by each of the four ECs is characterized at a fixed distance of 10 mm from the coil end face, with the current varying from 0 to 1 A. Both simulation and experimental results are plotted in Fig.5(c), showing the relationship between coil current and magnetic field strength.

C. Orientation Error Analysis

By applying randomized currents, the SPM is actuated to span a wide range of orientations. The corresponding sensor measurements formed an ellipsoid distribution in 3D space. The calibration algorithm fits this ellipsoid and computes the inverse transformation to map the data onto a perfect sphere, thereby recovering the true orientation.

As shown in Fig.5(d), the orientation error decreased rapidly with increasing number of samples and converged to approximately 3°. Under unknown offset conditions, the final error is still comparable to that obtained with known offsets. To ensure measurement accuracy, 20 random data sets are collected prior to each experiment for initialization calibration.

After calibration, Fig.5(e) presents the rotation error for various angles between the SPM magnetic moment and the Z-axis, with the SPM fixed and only currents applied. Larger driving currents effectively reduced the deviation error, with the smallest errors observed for horizontal and near-vertical orientations, while the 30°–60° interval exhibited relatively larger errors.

D. Collaborative robot-assisted angular deflection

The pose of the flange is defined by its position $\mathbf{P}_F \in \mathbb{R}^3$ and orientation $\mathbf{R}_F \in \mathrm{SO}(3)$ relative to the world frame. The SPM is attached to the tool such that its center is located at a fixed offset along the tool's z-axis as shown in Fig.3. The vector from the flange frame origin to the SPM is $\mathbf{P}_{M/F} = \begin{bmatrix}0, 0, h\end{bmatrix}^\top$. The world-frame position of the SPM is given by the kinematic equation

$$\mathbf{P}_M = \mathbf{P}_F + \mathbf{R}_F \mathbf{P}_{M/F} \tag{20}$$

During the assisted angular deflection process, $\mathbf{P}_M$ must remain constant to ensure a consistent distance from the SPM to the workspace plane. The control objective is to align the tool's z-axis with the targeted direction $\mathbf{z}_{\text{target}}$

$$\mathbf{z}_{\text{target}} = \begin{bmatrix}\sin p \cos d \\ \sin p \sin d \\ \cos p\end{bmatrix} \tag{21}$$

Let $\mathbf{z}_0 = \mathbf{R}_{F0} \begin{bmatrix}0 & 0 & 1\end{bmatrix}^\top$ be the initial tool z-axis direction. The minimal rotation from $\mathbf{z}_0$ to $\mathbf{z}_{\text{target}}$ is determined by its rotation axis $\mathbf{k}$ and the angle θ

$$\begin{cases}\mathbf{k} = \frac{\mathbf{z}_0 \times \mathbf{z}_{\text{target}}}{\|\mathbf{z}_0 \times \mathbf{z}_{\text{target}}\|} \\ \theta = \arccos(\mathbf{z}_0 \cdot \mathbf{z}_{\text{target}})\end{cases} \tag{22}$$

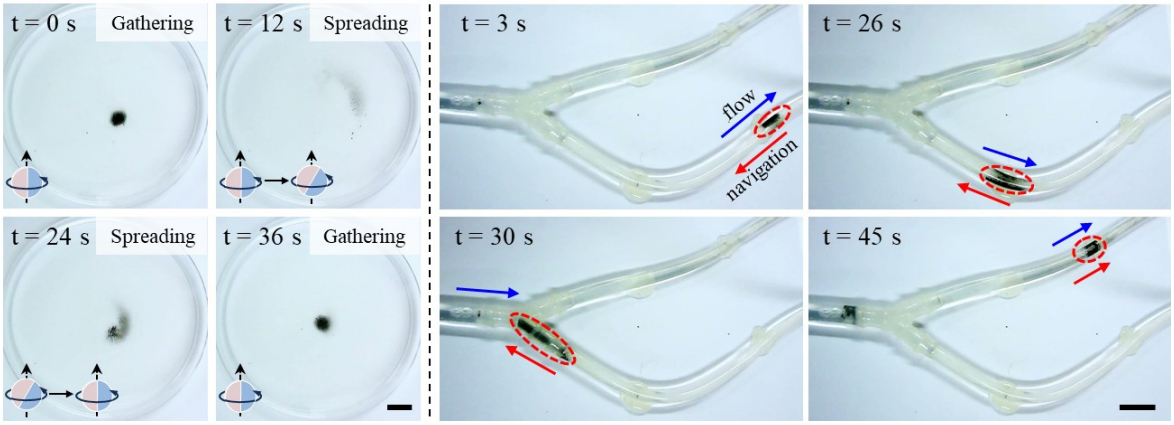

Fig. 7. Results of microswarm actuation in a static tank and a tube with fluid flow, respectively. (a) The four snapshots correspond to t = 0 s (gathering), t = 12 s (spreading), t = 24 s (spreading), and t = 36 s (gathering) under a variable rotating magnetic field. Insets in the lower left corner illustrates the rotating axis and direction of the SPM in the EPMA system beneath the work plane. (b) Targeted delivery of the microswarm under two different flow conditions. The blue and red arrow lines indicate the flow direction and the microswarm navigation direction, respectively. The positions of the microswarm during the delivery process are highlighted by red dashed circles. The tube flow rate is 60 mL/min. The interval t = 3–26 s corresponds to downstream conditions, and t = 30–45 s represents upstream conditions. The scale bars are 10 mm.

The incremental rotation matrix $\mathbf{R}_\Delta$ is constructed using Rodrigues' rotation formula

$$\mathbf{R}_\Delta = \mathbf{I} + (\sin\theta)[\mathbf{k}]_\times + (1-\cos\theta)[\mathbf{k}]_\times^2 \tag{23}$$

where $[\mathbf{k}]_\times$ is the skew-symmetric matrix of the vector $\mathbf{k}$. The targeted flange orientation is then found by applying this incremental rotation to the initial orientation

$$\mathbf{R}_{F1} = \mathbf{R}_\Delta \mathbf{R}_{F0} \tag{24}$$

The targeted flange position $\mathbf{P}_{F1}$ is computed inversely from the invariant constraint

$$\mathbf{P}_{F1} = \mathbf{P}_M - \mathbf{R}_{F1}\mathbf{P}_{M/F} \tag{25}$$

Under conditions requiring collaborative robot compensation, Fig.5(f) illustrates the variation in sweep distance for different deflection angle and SPM position. Increasing the deflection angle significantly enlarged the sweep distance. With $I_{\max} = 0.8\,\mathrm{A}$ and $P_{M/F} = 164\,\mathrm{mm}$, the sweep distance induced by auxiliary deflection remained below $0.4\,\mathrm{m}$.

IV. Experimental Results and Discussion

A. Microrobot delivery in complex terrains

This task aims to actuate a single microrobot through complex environments and accurately reach the targeted area (Fig.6(a)). The motion trajectory as shown in Fig.6(b), demonstrates that by flexibly adjusting the rotation direction of the magnetic field, multiple types of terrain delivery tasks can be accomplished.

In the obstacle overcoming scenario (Fig.6(c) ①–②), the microrobot is actuated to roll via the rotating magnetic field, while coordinated traction from the collaborative robot enables it to cross protrusions of varying widths. Subsequently, in the stair climbing scenario (Fig.6(c) ③), the rotation direction of the magnetic field is adjusted to align the motion of microrobot with the orientation of the stairs, thereby achieving step-by-step ascent and descent (Fig.6(c) ④).

During the narrow path crossing scenario (Fig.6(c) ⑤–⑥), precise control of the flipping angle is required to guide the microrobot into a narrow slit and complete turning within it. Finally, in the gap insertion scenario (Fig. 6(c) ⑦–⑧), the microrobot adjusts its rotation posture according to the gap position and, with the assistance of current actuation and fine-tuning by the collaborative robotic, is accurately inserted into the targeted gap.

B. Microswarm pattern control and delivery

Reversible pattern transformation of a magnetic microswarm is demonstrated in a static container, as illustrated in Fig.7(a). The container has a diameter of 85 mm, and 8 μg of particles are extracted from a 20% Fe_3O_4 and 1% PVP solution. Initially, a horizontally oriented rotating magnetic field at 4 Hz is applied, resulting in the formation of a stable microswarm. The microswarm is then spreading by adjusting the rotation axis of the SPM and gradually moving the collaborative robotic away from the working plane, thereby reducing the magnetic field gradient (t = 12 s). After spreading, the magnetic moment is returned to the horizontal direction and the collaborative robot is brought closer to the working plane, enabling the particles to regather into a compact and stable pattern of microswarm (t = 24–36 s).

Building upon this capability, targeted delivery experiment is performed in a Y-shaped tube with a constant flow rate of 60 mL/min to mimic physiological fluid conditions (Fig.7(b)). The main channel of the tube has an inner diameter of 3.5 mm, and the branch flow velocity is 52 mm/s. A total of 16 μg of particles is extracted from the same 20% Fe_3O_4 and 1% PVP solution. During the experiments, the SPM is rotated at a constant frequency of 4 Hz, while

the collaborative robot controls its position to actuate the microswarm.

The delivery task is as follows: the microswarm initiates movement from a downstream position in one branch (t = 3 s), overcomes fluid drag to traverse a curved segment (t = 26 s), and enters the bifurcation (t = 30 s). At the tube junction, the microswarm is steered into the selected branch and transported upstream to the targeted location (t = 45 s). These results confirm the EPMA system's capability for precise targeted delivery for microswarm in dynamic flow environments.

V. Conclusions

This work proposes the EPMA system that integrates an EC array and a SPM to enable the actuation and targeted delivery of various microrobots in diverse environments. Experimental results demonstrate that a single microrobot can be precisely actuated for obstacle overcoming, stair climbing, narrow path crossing, and gap insertion. Furthermore, microswarm actuation experiments validate the feasibility of microswarm reversible spreading-regathering by modulating the actuating magnetic field generated by the EPMA system. Magnetic delivery experiments in fluid environments further confirm the system's capability for effective microswarm navigation under both upstream and downstream flow conditions. The proposed EPMA system provides a MAS with highly controllable magnetic fields for actuating different types of microrobots, laying the groundwork for staged microrobotic delivery strategies and future biomedical applications.

References

[1] V. Iacovacci, E. Diller, D. Ahmed, and A. Menciassi, "Medical microrobots," *Annual Review of Biomedical Engineering*, vol. 26, no. 1, pp. 561–591, 2024.

[2] Q. Boehler, S. Gervasoni, S. L. Charreyron, C. Chautems, and B. J. Nelson, "On the workspace of electromagnetic navigation systems," *IEEE Transactions on Robotics*, vol. 39, no. 1, pp. 791–807, 2022.

[3] S. Zhong, Z. Xin, Y. Hou, Y. Li, H.-W. Huang, T. Sun, Q. Shi, and H. Wang, "Double-modal locomotion of a hydrogel ultra-soft magnetic miniature robot with switchable forms," *Cyborg and Bionic Systems*, vol. 5, p. 0077, 2024.

[4] A. W. Mahoney and J. J. Abbott, "Generating rotating magnetic fields with a single permanent magnet for propulsion of untethered magnetic devices in a lumen," *IEEE Transactions on Robotics*, vol. 30, no. 2, pp. 411–420, 2013.

[5] R. Nauber, S. R. Goudu, M. Goeckenjan, M. Bornhäuser, C. Ribeiro, and M. Medina-Sánchez, "Medical microrobots in reproductive medicine from the bench to the clinic," *Nature Communications*, vol. 14, no. 1, p. 728, 2023.

[6] Q. Wang, D. Jin, B. Wang, N. Xia, H. Ko, B. Y. M. Ip, T. W. H. Leung, S. C. H. Yu, and L. Zhang, "Reconfigurable magnetic microswarm for accelerating tpa-mediated thrombolysis under ultrasound imaging," *IEEE/ASME Transactions on Mechatronics*, vol. 27, no. 4, pp. 2267–2277, 2021.

[7] A. J. Sperry, T. J. Schwehr, E. K. Pinegar, O. B. Richards, J. D. Rolston, M. D. Alexander, B. Coats, J. J. Abbott, and A. Kuntz, "Screw-tip soft magnetically steerable needles," *IEEE Transactions on Medical Robotics and Bionics*, vol. 6, no. 1, pp. 4–17, 2023.

[8] D. Jin, Q. Wang, K. F. Chan, N. Xia, H. Yang, Q. Wang, S. C. H. Yu, and L. Zhang, "Swarming self-adhesive microgels enabled aneurysm on-demand embolization in physiological blood flow," *Science Advances*, vol. 9, no. 19, p. eadf9278, 2023.

[9] R. Dreyfus, Q. Boehler, S. Lyttle, P. Gruber, J. Lussi, C. Chautems, S. Gervasoni, J. Berberat, D. Seibold, N. Ochsenbein-Kölble, *et al.*, "Dexterous helical magnetic robot for improved endovascular access," *Science Robotics*, vol. 9, no. 87, p. eadh0298, 2024.

[10] R. Xu, X. Wang, Y. Chen, L. M. Tam, and Q. Xu, "Bio-inspired magnetic soft robots with omnidirectional climbing for multifunctional biomedical applications," *International Journal of Extreme Manufacturing*, 2025.

[11] Y. Huo, L. Yang, T. Xu, and D. Sun, "Design, control, and clinical applications of magnetic actuation systems: Challenges and opportunities," *Advanced Intelligent Systems*, vol. 7, no. 3, p. 2400403, 2025.

[12] X. Du and J. Yu, "Image-integrated magnetic actuation systems for localization and remote actuation of medical miniature robots: A survey," *IEEE Transactions on Robotics*, vol. 39, no. 4, pp. 2549–2568, 2023.

[13] Y. Ma, X. An, Q. Yang, M. Cai, Z. Tang, J. Chang, V. Iacovacci, T. Xu, L. Zhang, and Q. Wang, "Magnetic continuum robot for intelligent manipulation in medical applications," *SmartBot*, p. e12011, 2025.

[14] A. Z. Taddese, P. R. Slawinski, M. Pirotta, E. De Momi, K. L. Obstein, and P. Valdastri, "Enhanced real-time pose estimation for closed-loop robotic manipulation of magnetically actuated capsule endoscopes," *The International Journal of Robotics Research*, vol. 37, no. 8, pp. 890–911, 2018.

[15] L. Yang, M. Zhang, Z. Yang, and L. Zhang, "Multimode control of a parallel-mobile-coil system for adaptable large-workspace microrobotic actuation," *IEEE/ASME Transactions on Mechatronics*, vol. 28, no. 3, pp. 1662–1673, 2022.

[16] A. J. Petruska and J. J. Abbott, "Omnimagnet: An omnidirectional electromagnet for controlled dipole-field generation," *IEEE Transactions on Magnetics*, vol. 50, no. 7, pp. 1–10, 2014.

[17] F. Niu, J. Li, W. Ma, J. Yang, and D. Sun, "Development of an enhanced electromagnetic actuation system with enlarged workspace," *IEEE/ASME Transactions on Mechatronics*, vol. 22, no. 5, pp. 2265–2276, 2017.

[18] H. Lee, N. L. Gharamaleki, and H. Choi, "Open-loop position control of a miniature magnetic robot using two-dimensional divergence control of a magnetic force," in *2025 IEEE International Conference on Robotics and Automation (ICRA)*. IEEE, 2025, pp. 9068–9073.

[19] X. Du, M. Zhang, J. Yu, L. Yang, P. W. Y. Chiu, and L. Zhang, "Design and real-time optimization for a magnetic actuation system with enhanced flexibility," *IEEE/ASME Transactions on Mechatronics*, vol. 26, no. 3, pp. 1524–1535, 2020.

[20] M. P. Kummer, J. J. Abbott, B. E. Kratochvil, R. Borer, A. Sengul, and B. J. Nelson, "Octomag: An electromagnetic system for 5-dof wireless micromanipulation," *IEEE Transactions on Robotics*, vol. 26, no. 6, pp. 1006–1017, 2010.

[21] J. Sikorski, C. M. Heunis, F. Franco, and S. Misra, "The armm system: An optimized mobile electromagnetic coil for non-linear actuation of flexible surgical instruments," *IEEE Transactions on magnetics*, vol. 55, no. 9, pp. 1–9, 2019.

[22] J. Yu, L. Yang, and L. Zhang, "Pattern generation and motion control of a vortex-like paramagnetic nanoparticle swarm," *The International Journal of Robotics Research*, vol. 37, no. 8, pp. 912–930, 2018.

[23] S. E. Wright, A. W. Mahoney, K. M. Popek, and J. J. Abbott, "The spherical-actuator-magnet manipulator: A permanent-magnet robotic end-effector," *IEEE Transactions on Robotics*, vol. 33, no. 5, pp. 1013–1024, 2017.

[24] P. Ryan and E. Diller, "Magnetic actuation for full dexterity microrobotic control using rotating permanent magnets," *IEEE Transactions on Robotics*, vol. 33, no. 6, pp. 1398–1409, 2017.

[25] G. Pittiglio, M. Brockdorff, T. da Veiga, J. Davy, J. H. Chandler, and P. Valdastri, "Collaborative magnetic manipulation via two robotically actuated permanent magnets," *IEEE Transactions on Robotics*, vol. 39, no. 2, pp. 1407–1418, 2022.

[26] X. Fan, Y. Jiang, M. Li, Y. Zhang, C. Tian, L. Mao, H. Xie, L. Sun, Z. Yang, and M. Sitti, "Scale-reconfigurable miniature ferrofluidic robots for negotiating sharply variable spaces," *Science Advances*, vol. 8, no. 37, p. eabq1677, 2022.

[27] J. J. Abbott, E. Diller, and A. J. Petruska, "Magnetic methods in robotics," *Annual Review of Control, Robotics, and Autonomous Systems*, vol. 3, no. 1, pp. 57–90, 2020.

[28] J. Fang, H. Sun, J. Cao, X. Zhang, and Y. Tao, "A novel calibration method of magnetic compass based on ellipsoid fitting," *IEEE Transactions on Instrumentation and Measurement*, vol. 60, no. 6, pp. 2053–2061, 2011.